Supplementary Information (SI) for Journal of Materials Chemistry A.

Supporting information (SI) for

Ultrasound-Assisted Directional Freezing Enables High-Performance Hydrogel Evaporators with Tunable Microchannels for Solar Desalination

Shanbin Zhang[1], Hang Su[1], Limei Li[1], Jianbin Ma[1], Zhenyu Wang[1], Fangqiu Hu[1], Yujun Sun[1], Jitian Song[1,*]

[1]Tianjin Key Laboratory of Integrated Design and On-line Monitoring for Light Industry & Food Machinery and Equipment, College of Mechanical Engineering, Tianjin University of Science and Technology, Tianjin, 300222, China

*Corresponding authors.

E-mail addresses: songjt@tust.edu.cn

Preparation of PVA/CS Precursor Solution (for a 100 mL Batch)

To prepare the PVA/CS precursor solution (taking 100 mL as an example), a 9 wt% PVA aqueous solution was first prepared by dissolving 2.25 g of PVA in 22.75 mL of deionized water under magnetic stirring at 90 °C for 1 hour until completely dissolved. Then, a 2 wt% CS solution was prepared by adding 1.5 g of low-molecular-weight chitosan to 70 mL of water, followed by the addition of 3.7 mL of phosphoric acid. The mixture was stirred at 80 °C for 30 minutes until fully dissolved, after which 0.75 mL of phytic acid (50 wt% aqueous solution) was added and stirring was continued until homogeneous. The PVA and CS solutions were then mixed thoroughly in a mass ratio of 1:3 (9 wt% PVA solution to 2 wt% CS solution). Subsequently, 1.0 g of conductive CB powder was added to the mixed solution and stirred thoroughly, followed by ultrasonic treatment to ensure uniform dispersion. Finally, 50 wt% glutaraldehyde solution was added to initiate crosslinking, and the mixture was left undisturbed for 30 minutes to obtain the final PVA/CS precursor solution.

Characterization

The surface morphology of freeze-dried hydrogel samples was characterized using a scanning electron microscope (SEM, SU3800, Hitachi, Japan). Elemental analysis of the hydrogels was conducted using an energy-dispersive X-ray spectrometer (EDS, Oxford Ultim Max65, UK). The pore size and its distribution were analyzed with ImageJ software. The wettability of the hydrogels was evaluated using a contact angle goniometer (OCA15EC, Dataphysics, Germany) with 5 μL of deionized water as the test droplet. The light absorption properties of the hydrogels were precisely measured using a UV-Vis-NIR spectrophotometer (SHIMADZU UV-3600i Plus, Japan) equipped with an integrating sphere over the wavelength range of 250-2500 nm. Metal ion concentrations in the collected water were determined by inductively coupled plasma optical emission spectrometry (ICP-OES, PerkinElmer Optima 8000). Thermal behaviors such as melting and evaporation of the hydrogels were studied using differential scanning calorimetry (DSC, TA-Discovery, USA), where the sample was heated from 25 °C to 130 °C at a rate of 5 °C /min under a nitrogen atmosphere. The state of water molecules in the hydrogel was further analyzed via Raman spectroscopy (HORIBA LabRAM HR Evolution, Japan) using a 532 nm excitation wavelength. The compressive mechanical properties of the hydrogels were tested using a universal testing machine (UTM4103, China).

Solar Vapor Generation (SVG) Test

The solar-driven water evaporation performance was evaluated under simulated sunlight using a xenon lamp (PLS-SXE 300+, Perfectlight, China), which provided an output power equivalent to one sun (1 kW m^{-2}). The illumination intensity was monitored and calibrated using a connected power meter (PLD MOPM-I, Perfectlight, China). During testing, a CPC-UA hydrogel sample with a thickness of approximately 1 cm was placed on a polystyrene (PS) foam support within a beaker. The water in the beaker was either deionized water or contaminated water (used for purification experiments). A laboratory electronic balance with a resolution of 0.1 mg (JA2003, Soptop) was used to record the mass loss of bulk water. All experiments were conducted under controlled environmental conditions: an ambient temperature of 21 °C and relative humidity of 25 %. The evaporation rate was measured after the system reached a steady state under one sun illumination for 30 minutes. Outdoor evaporation experiments were performed at the Binhai Campus of Tianjin University of Science and Technology from July 7 to July 9. The solar-to-vapor energy conversion efficiency (η, %) was calculated using the following equation:

$$\eta = \frac{m h_{water}}{3600 I} \tag{S1}$$

where m (kg m^{-2} h^{-1}) is the net evaporation rate after subtracting the dark evaporation rate, h_{water} (kJ kg^{-1}) is the enthalpy of water evaporation, and I (kW m^{-2}) is the incident solar irradiance.

Contact Angle (CA) Measurement

The wettability of the hydrogel samples was evaluated using an optical contact angle goniometer (Dataphysics, Germany). A 5 μL droplet of deionized water was deposited onto the hydrogel surface, and the spreading and absorption processes were recorded by a high-speed camera. The reported contact angle (CA) values represent the average of three measurements taken at different positions on each hydrogel surface.

Photothermal Performance Test

The photothermal properties of different samples were evaluated under one sun irradiation using a xenon lamp (PLS-SXE 300+, Perfectlight, China). During illumination, the surface temperature of each sample was monitored in real time using an infrared thermal imaging camera (H10, HIKVISION).

Mechanical Compression Test

The compressive properties of the hydrogel samples were evaluated using a universal testing machine (UTM4103, China) at a loading rate of 1 mm/s. The stress-strain behavior was recorded under varying strain conditions.

Salt Tolerance and Performance in Dye and Acid/Base Solutions

To simulate seawater with different salinities, NaCl solutions with varying concentrations (3.5, 7, 10, 15, 20, and 25 wt%) were prepared. The evaporation devices containing different hydrogel samples were placed in these solutions for testing.

For organic pollutant removal tests, three typical industrial dyes—methylene blue (MB), methyl orange (MO), and rhodamine B (RhB) were each dissolved to form 2 vol% solutions. Additionally, 1 mol/L NaOH and 1 mol/L HCl solutions were prepared to evaluate the chemical stability of the hydrogels under strong alkaline and acidic conditions. The evaporation performance was tested following the same procedures as described above, with the saline solution replaced by the corresponding test liquids.

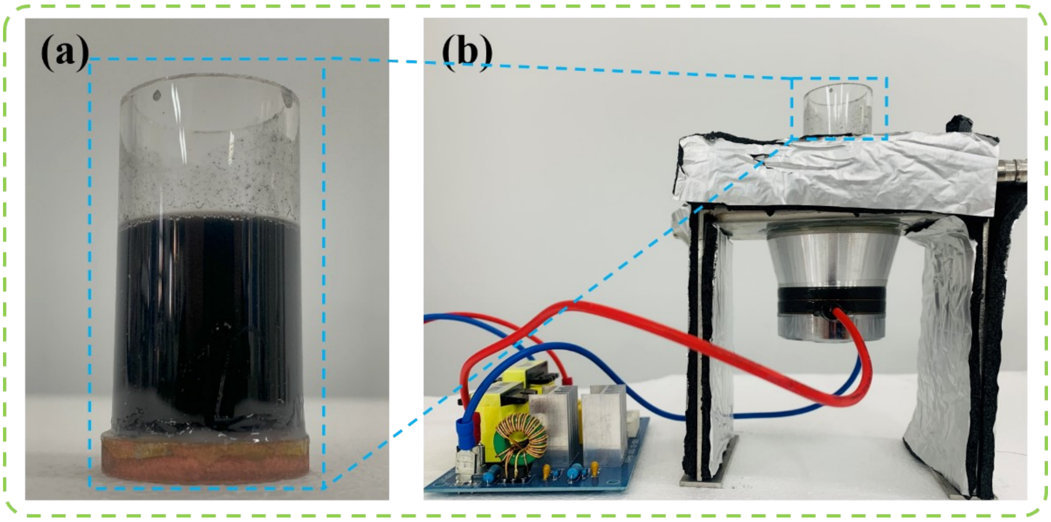

Figure S1. (a) Photograph of the mold containing hydrogel. (b) Photograph of the directional freezing apparatus.

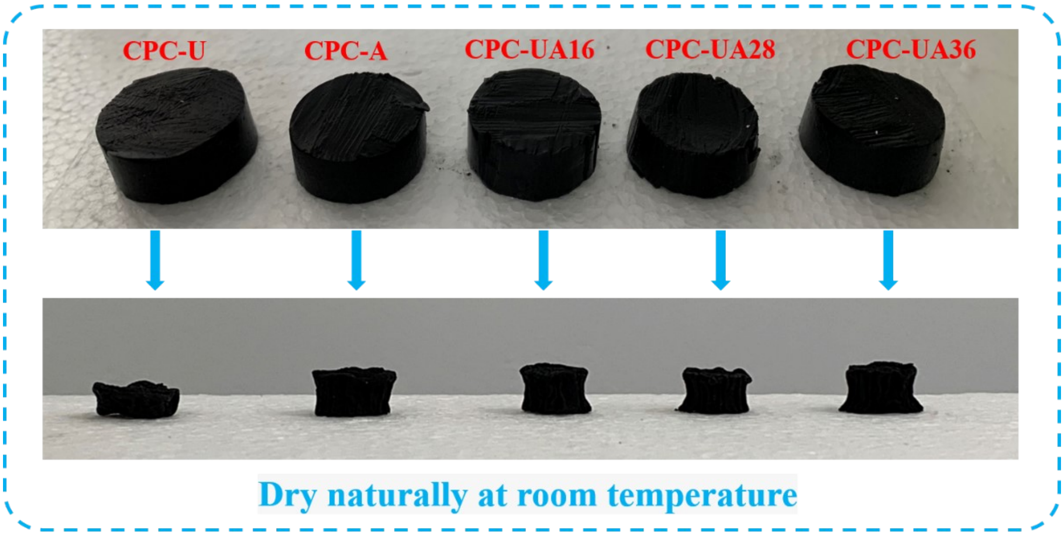

Figure S2. Photographs of hydrogel samples before and after drying at room temperature.

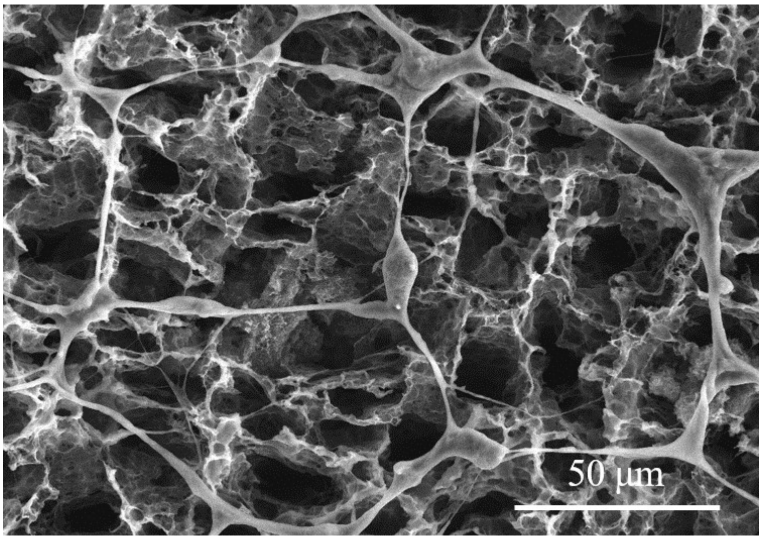

Figure S3. SEM images of hydrogels prepared by ultrasound-assisted directional freezing.

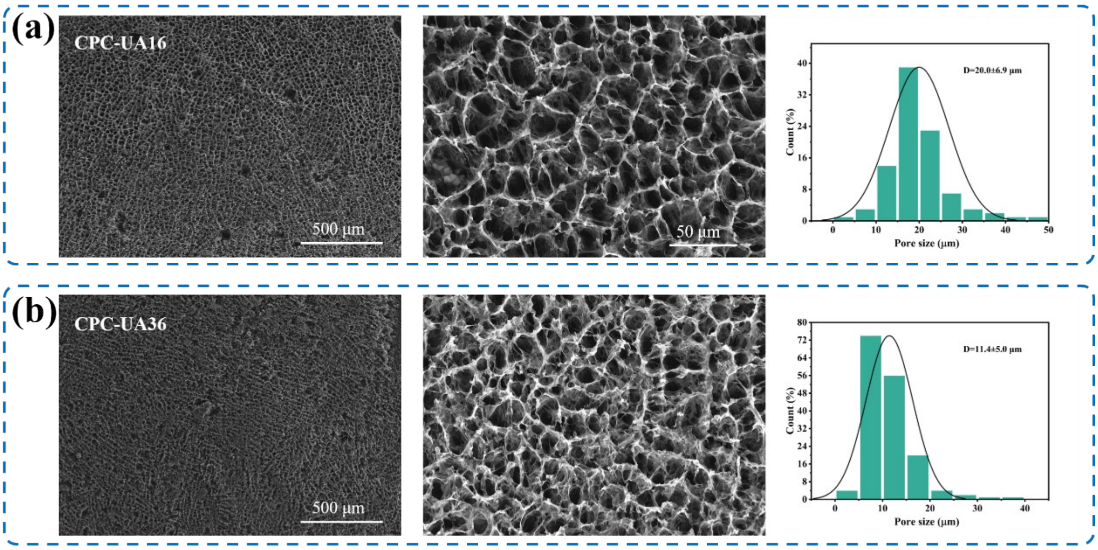

Figure S4. (a) SEM micrograph and pore size distribution of CPC-UA16. (b) SEM micrograph and pore size distribution of CPC-UA

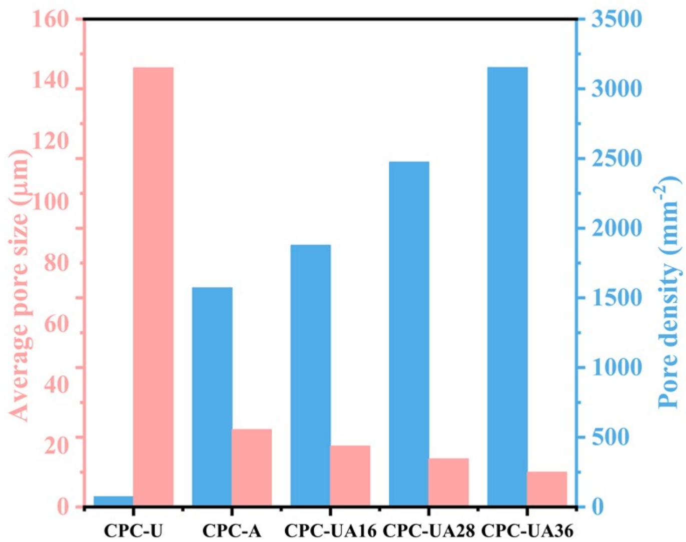

Figure S5. Pore size distribution and pore density of the hydrogels.

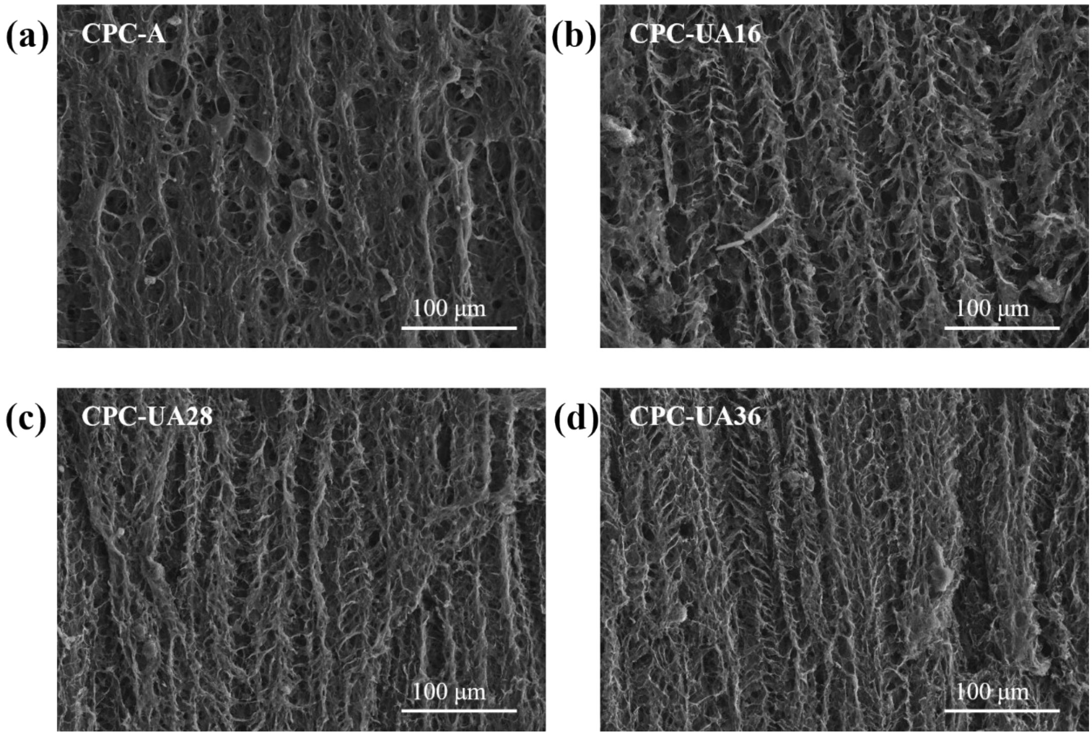

Figure S6. SEM cross-sectional images of vertically sliced hydrogels: (a) CPC-A, (b) CPC-UA16, (c) CPC-UA28, (d) CPC-UA36.

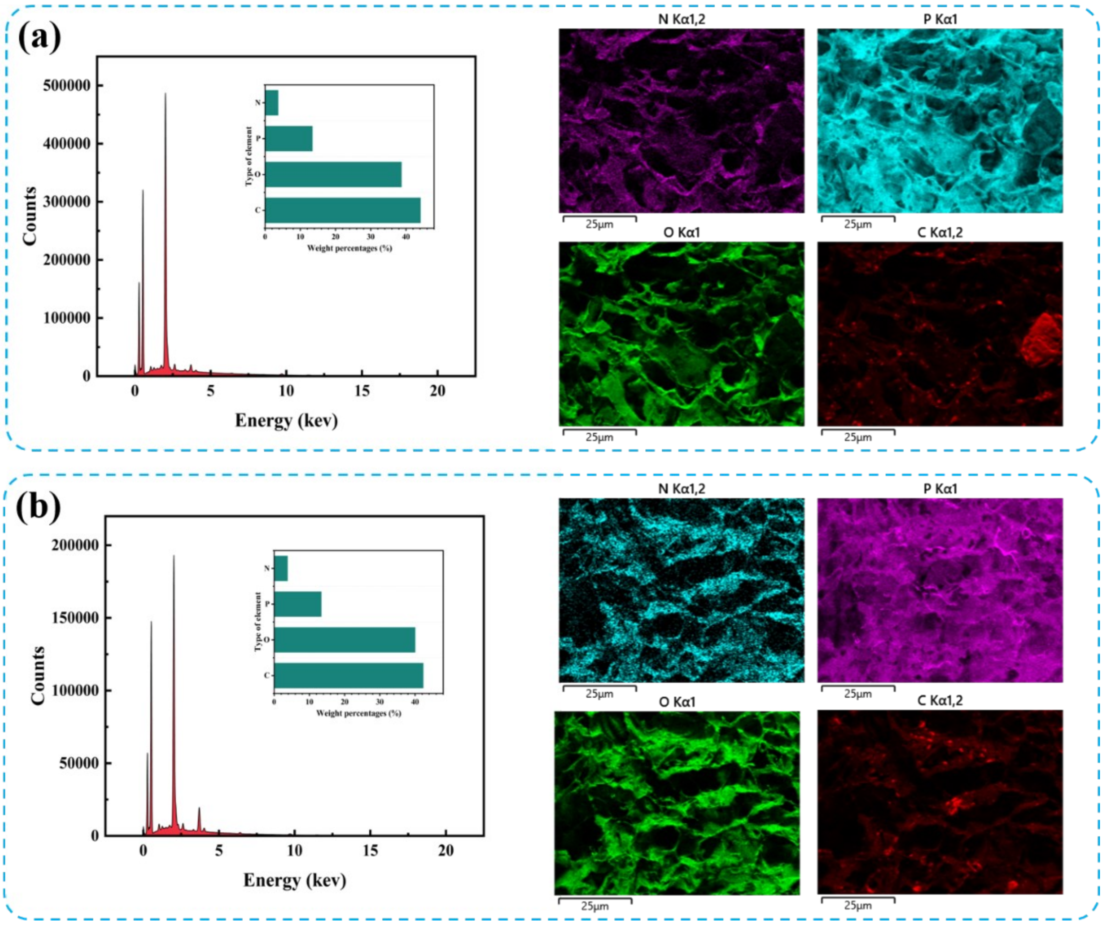

Figure S7. (a) EDS mapping and elemental distribution of CPC-A. (b) EDS mapping and elemental distribution of CPC-UA28.

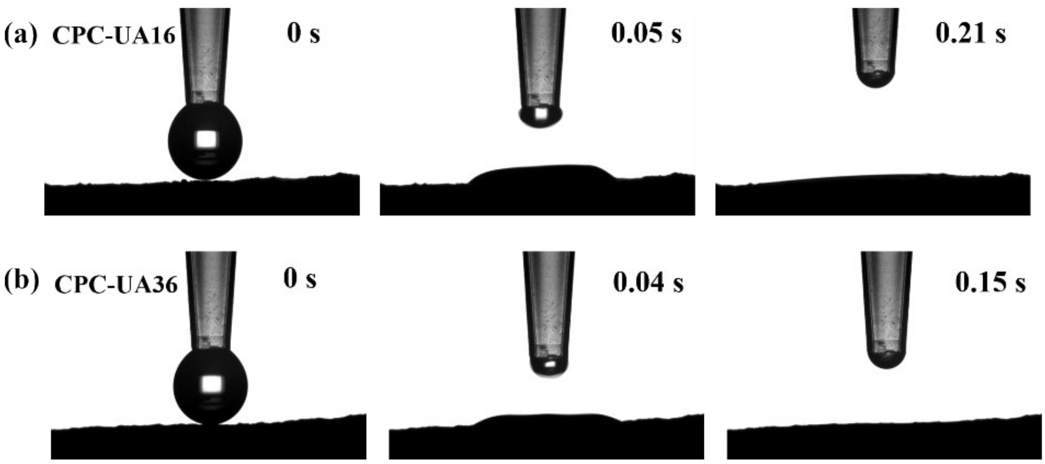

Figure S8. Contact angle images of: (a) CPC-UA16, (b) CPC-UA36.

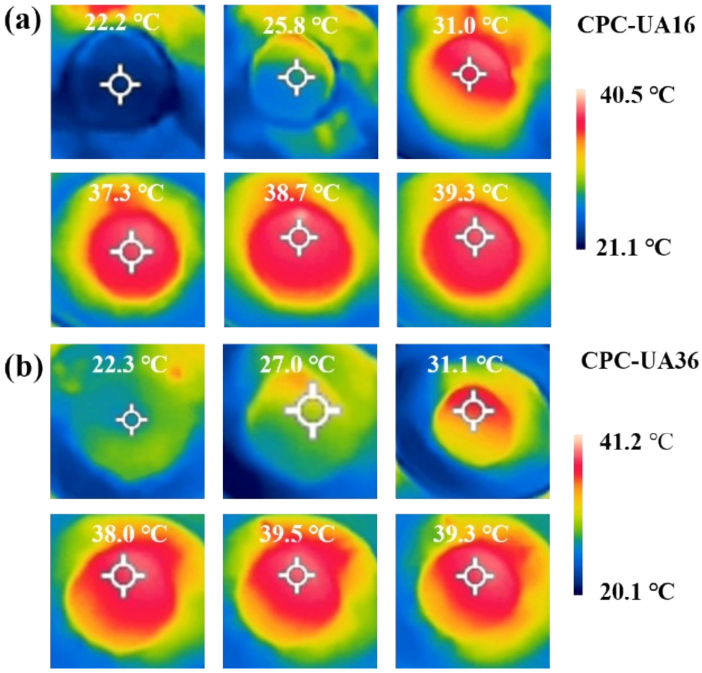

Figure S9. Infrared thermographic images of: (a) CPC-UA16, (b) CPC-UA36.

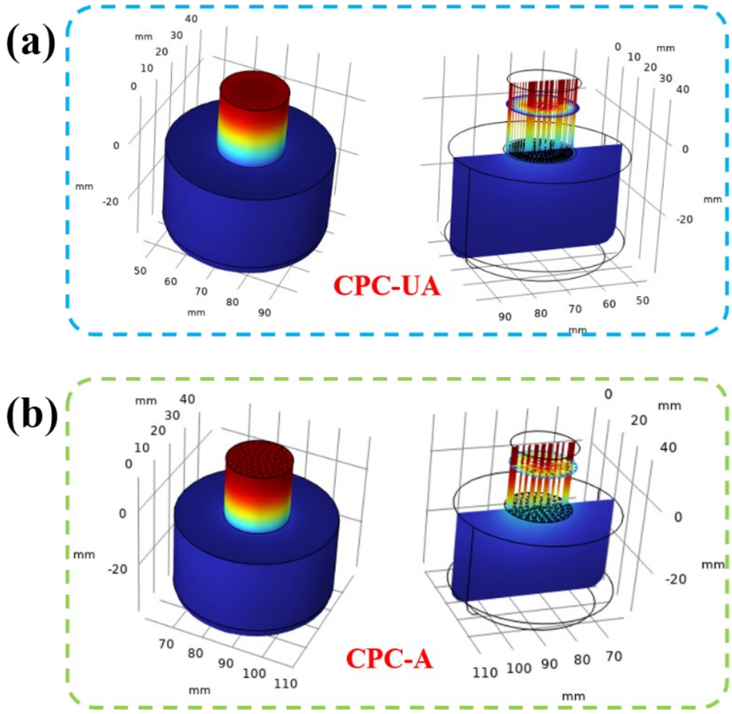

Figure S10. (a, b) Simulated temperature distribution and cross-sectional view of CPC-UA and CPC-A by COMSOL.

Figure S11. Macroscopic compression images of CPC-U, CPC-A, and CPC-UA28.

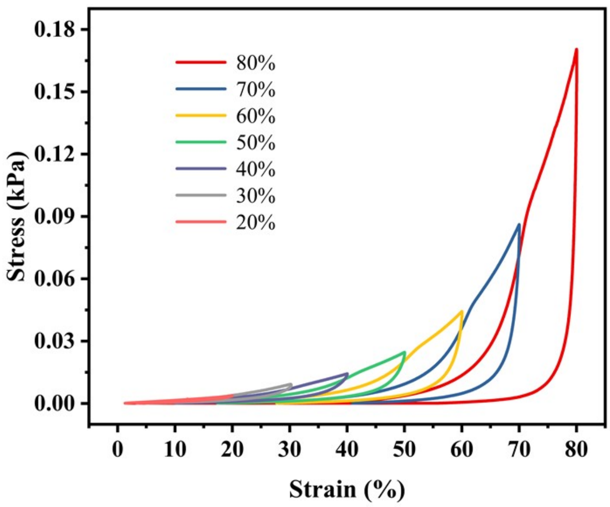

Figure S12. Stress–strain curves of CPC-UA28 under loading and unloading with strain increments of 10% up to 80%.

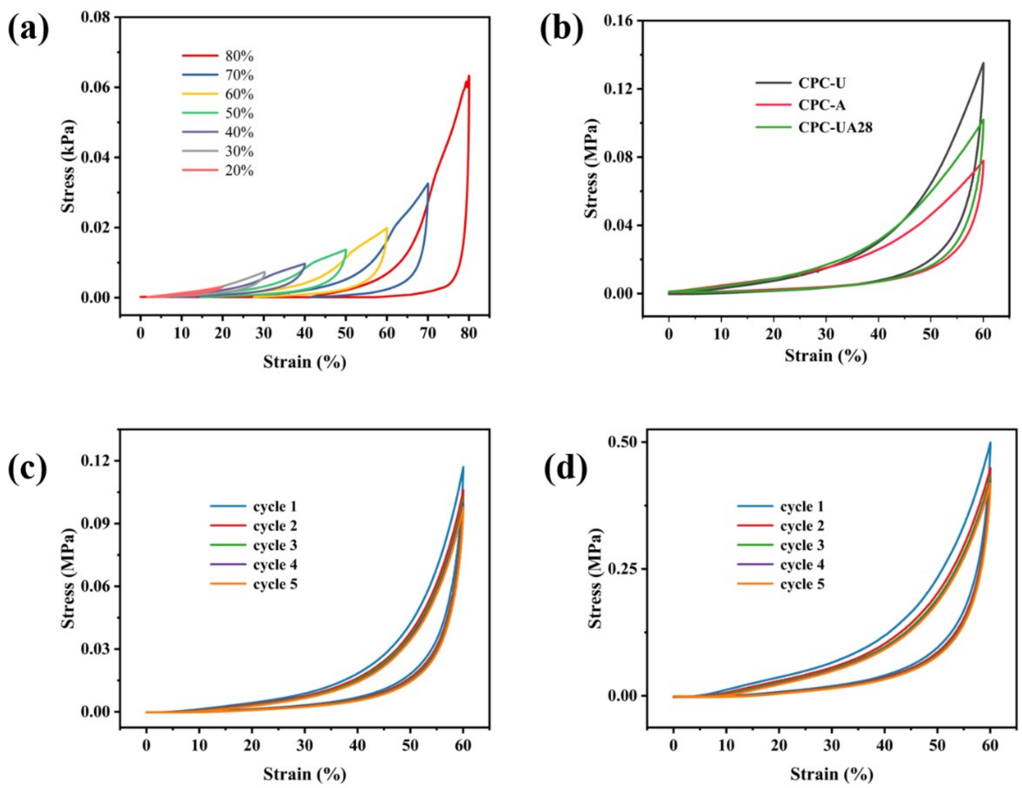

Figure S13. (a) Stress–strain curves of CPC-A under stepwise loading/unloading from 10% to 80% strain. (b) Comparison of compressive stress–strain curves of CPC-U, CPC-A, and CPC-UA28 under 0-60% strain. (c) Cyclic compressive stress–strain curves of CPC-U at a fixed strain of 60%. (d) Cyclic compressive stress–strain curves of CPC-A at a fixed strain of 60%.

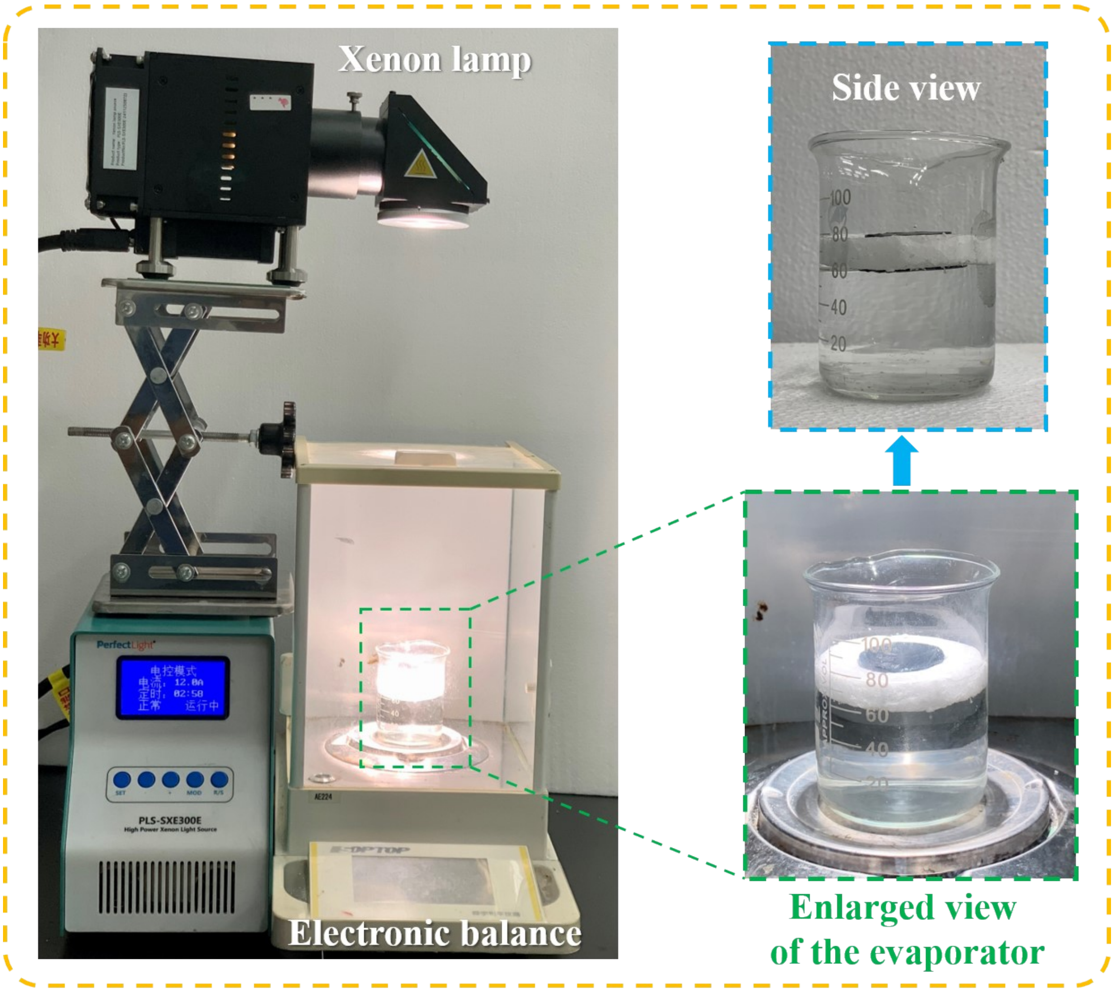

Figure S14. Photographs of the indoor test setup and interfacial evaporation system.

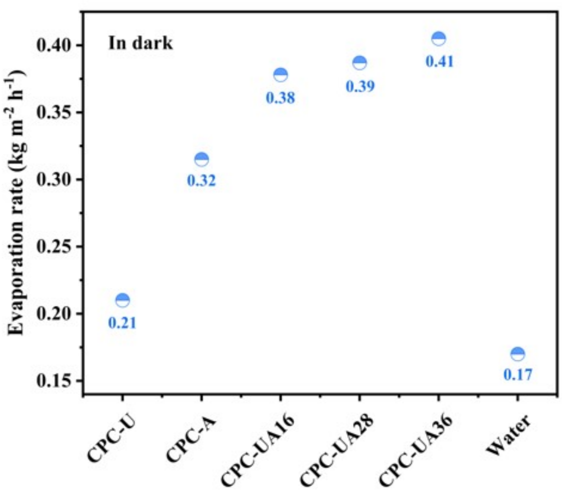

Figure S15. Evaporation rates of various hydrogels under dark conditions.

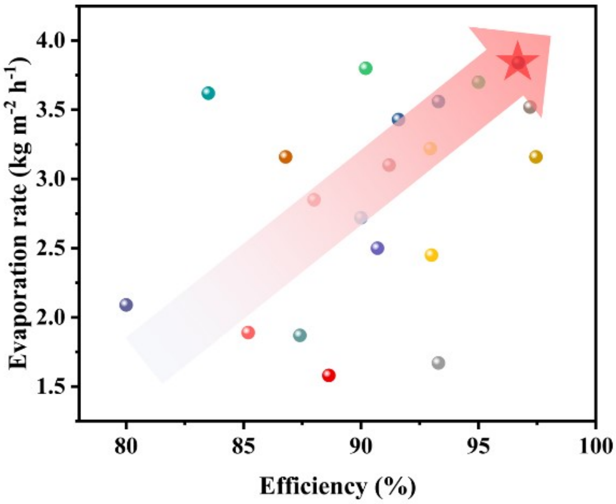

Figure S16. Comparison of evaporation rate and solar evaporation efficiency of different hydrogels under 1 sun illumination.

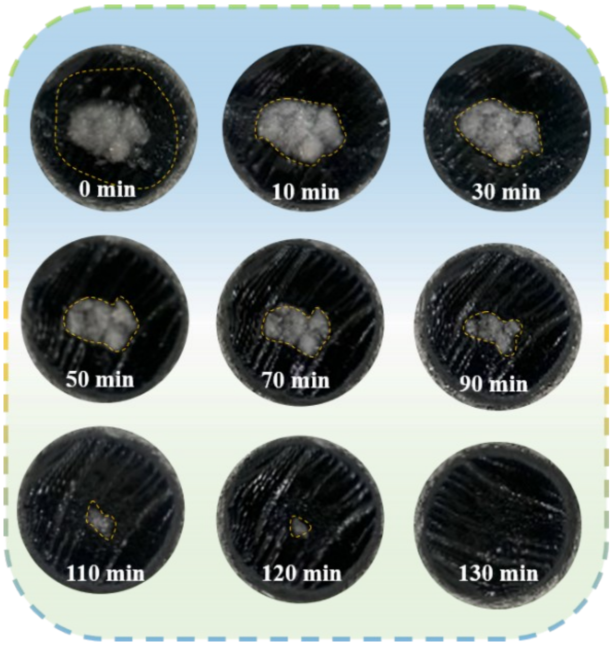

Figure S17. Dissolution process of 1 g NaCl on the surface of CPC-UA28 hydrogel.

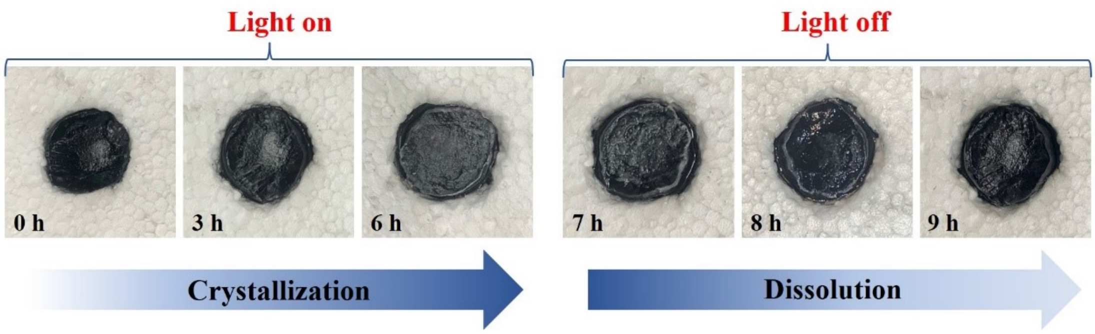

Figure S18. Photographs of salt crystallization and dissolution on CPC-UA36 during evaporation in 25 wt% saline water under one-sun illumination.

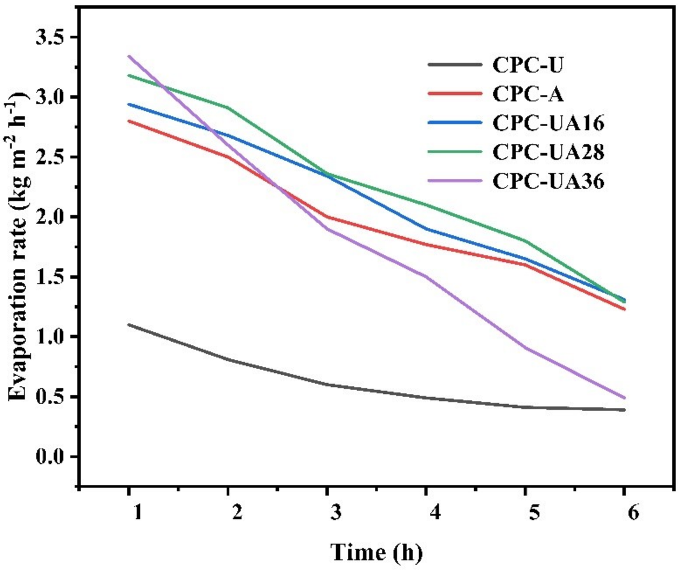

Figure S19. Variation of evaporation rates of different hydrogels in 25 wt% saline water under one-sun illumination.

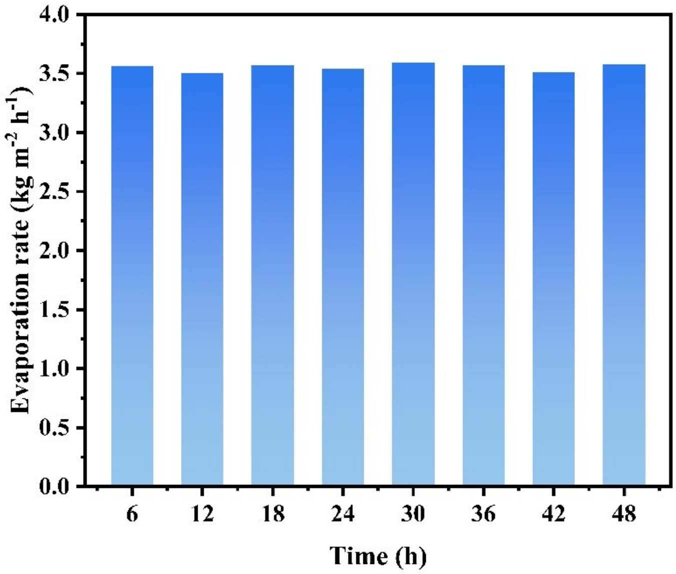

Figure S20. Evaporation rate variation of CPC-UA28 during continuous 48 h seawater evaporation under one-sun illumination.

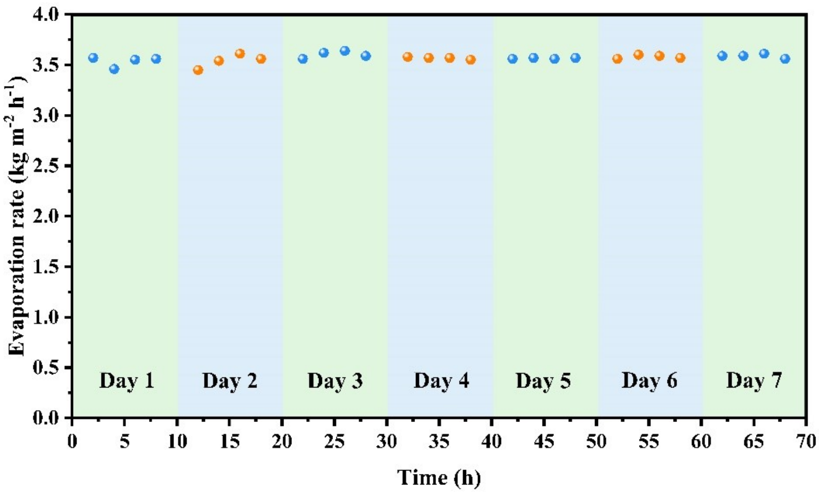

158

159 **Figure S21.** Seven-day cycling stability test of CPC-UA28 in seawater under one-sun

160 illumination, with each cycle lasting 8 h.

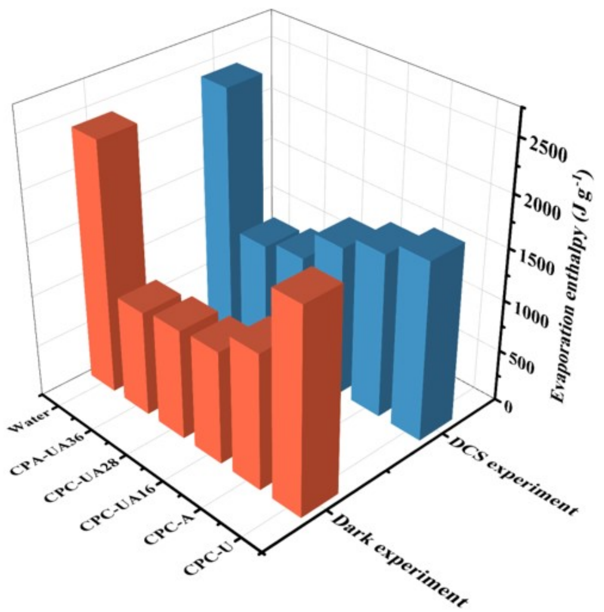

161

162 **Figure S22.** Comparison between DSC-derived evaporation enthalpy and dark-

163 condition-derived evaporation enthalpy of various hydrogels.

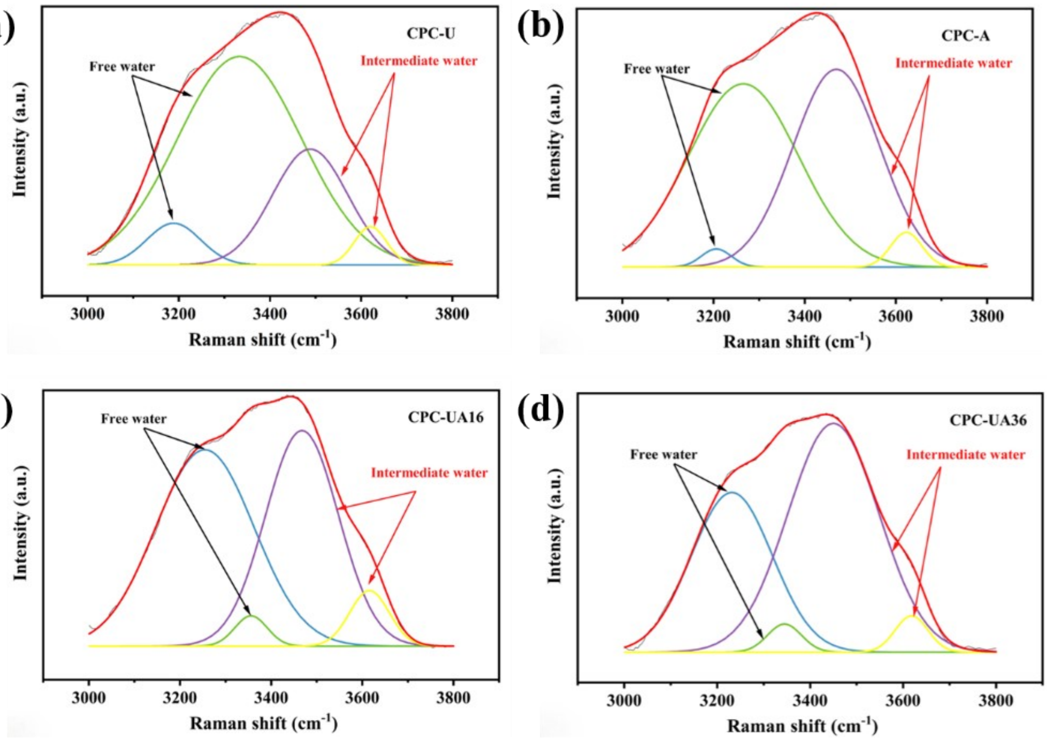

Figure S23. Raman spectra of: (a) CPC-U, (b) CPC-A, (c) CPC-UA16, (d) CPC-UA36.

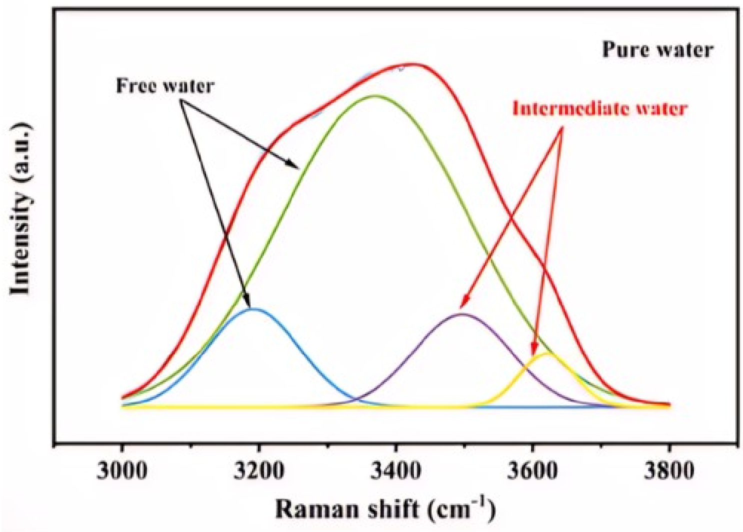

IW/FW=0.1768

Figure S24. Raman spectrum of pure water and the IW/FW ratio.

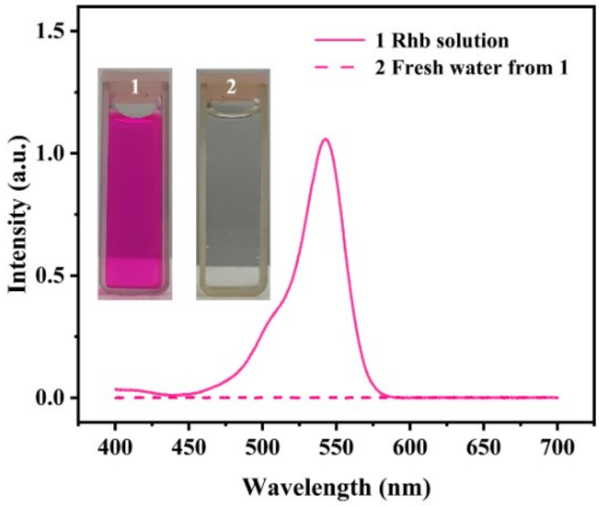

Figure S25. UV-vis absorption spectra of Rhodamine B (RhB) contaminated water and the collected distilled water.

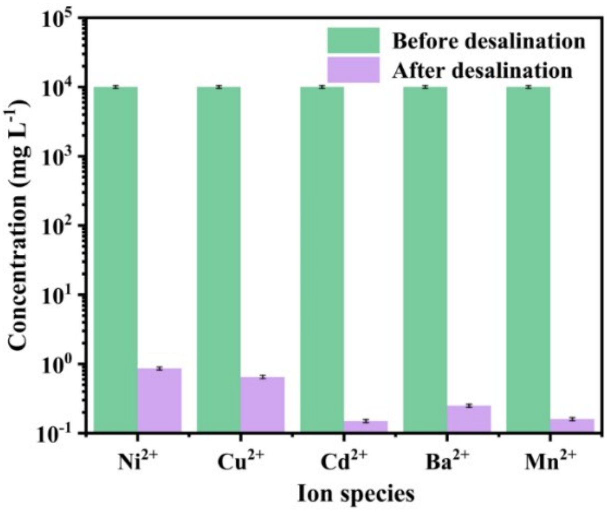

Figure S26. Heavy metal ion concentrations in simulated wastewater before and after solar desalination.

Figure S27. Photograph of mildew in peas farmed with seawater.

Figure S28. Photographs showing the pH values of 1 M NaOH, 1 M HCl, and distilled water.

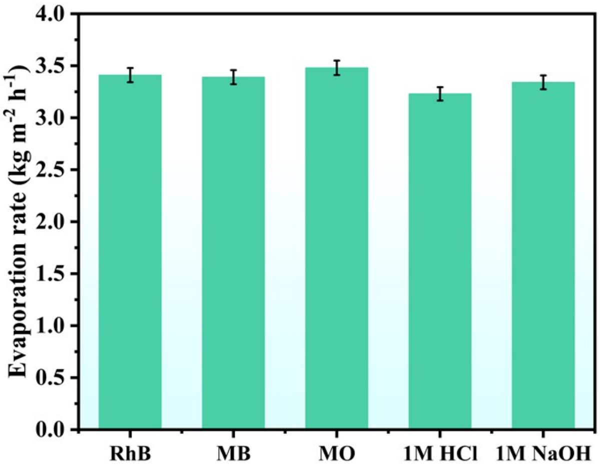

Figure S29. Evaporation rates of CPC-UA28 in different dye wastewater and acid/base solutions.

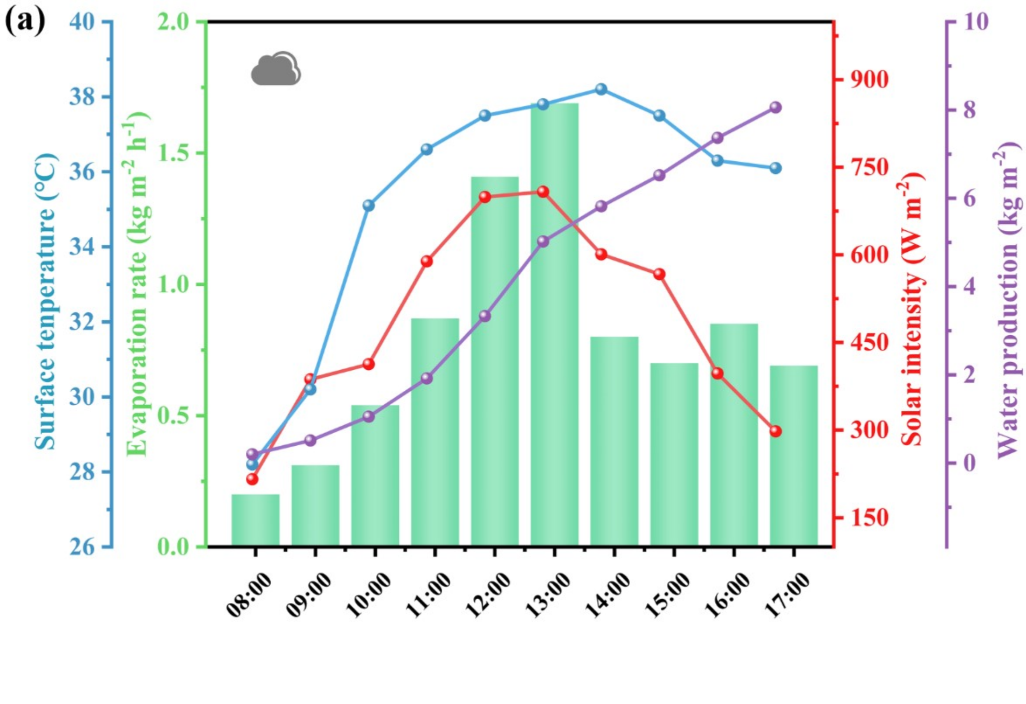

(b)

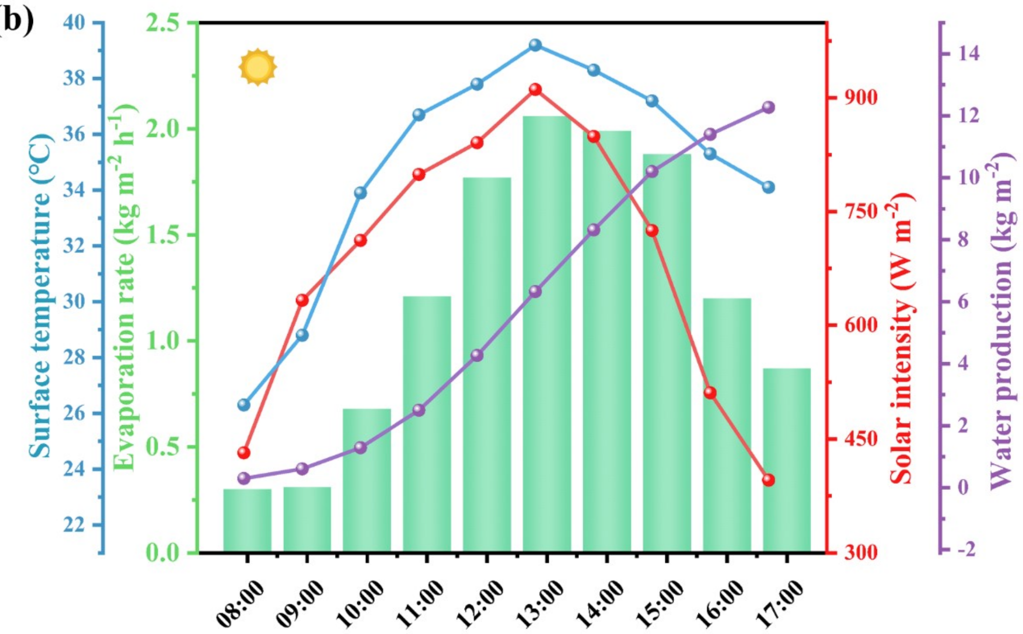

185

186 **Figure S30.** In the outdoor experiments on July 8 (a) and 9 (b), 2025, CPC-UA28 recorded freshwater production, cumulative freshwater production, surface temperature, evaporation rate, and light intensity.

189

Table S1 Tensile mechanical properties of hydrogels.

Name	Tensile strength(MPa)	Elastic modulus(MPa)	Elongation at break(%)
CPC-U	0.08	0.06	135.2
CPC-A	0.11	0.08	176.4
CPC-UA28	0.13	0.09	181.9

Table S2 Comparison of Evaporation Rate and Efficiency of CPC-UA28 with Reported Hydrogel-Based Evaporators under One Sun Irradiation.

Entry	Photothermal material	Evaporation rate ($kg\ m^{-2}\ h^{-1}$)	Efficiency (%)	Reference in SI
1	Directed ultrasound freezing of CB/PVA-CS hydrogels	3.84	96.7	This work
2	CB/Nano-silica PVA-CS	1.58	88.63	[1]
3	AC/Janus PVA-AG	3.56	93.3	[2]
4	3D LSC5/PVA-CS	2.45	93.0	[3]
5	CNTs-PVA/TOCNFs/SLS	3.70	95.0	[4]
6	Carbon nanotube PVA/SLS	2.09	80.0	[5]
7	PVA/CS/GO-Ag-4%EFMs	1.67	93.3	[6]
8	PVA biochar hydrogels	1.89	85.2	[7]
9	Janus PSPH@CP	2.72	90.0	[8]
10	CNTs and Chinese ink cellulose/PVA	3.16	86.79	[9]
11	MXene/rGO-embedded	3.62	83.5	[10]

	hybrid hydrogels			
12	δ-MnO_2-PVA composite hydrogels	2.5	90.7	[11]
13	PVA-CB	3.52	97.2	[12]
14	MWCNTs/PVA-agar	3.1	91.2	[13]
15	3D-GO/PVA	1.87	87.4	[14]
16	3D PVA/PDA	3.16	97.45	[15]
17	PVA fabric interpenetrating composite hydrospongels	2.85	88	[16]
18	ACNTs-PDA/PVA PPCHs	3.43	91.6	[17]
19	MoS_2-PVA/P(SA)	3.22	92.95	[18]
20	CNPs-PVA/CS	3.80	\	[19]

Table S3 Average pore size and salt crystallization rate of different hydrogels.

<table>
<tr><th>Name</th><th>Pore structure</th><th>Average pore size(μm)</th><th>Salt Accumulation</th></tr>
<tr><td>CPC-U</td><td>Random Porous Network</td><td>144</td><td>
</td></tr>
<tr><td>CPC-A</td><td rowspan="3">Vertical Channel</td><td>25.36</td><td>
</td></tr>
<tr><td>CPC-UA16</td><td>19.97</td><td>
</td></tr>
<tr><td>CPC-UA28</td><td>15.79</td><td>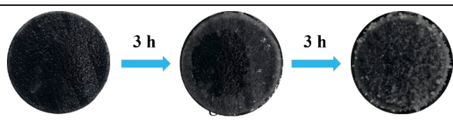
</td></tr>
</table>

CPC-UA36		11.43	

Table S4 Comparison of Enthalpy of Vaporization Measured by DSC and Estimated from Dark Evaporation Experiments.

Evaporation enthalpy(J/g)	CPC-U	CPC-A	CPC-UA16	CPC-UA28	CPC-UA36	Pure water
DSC measurement	1726.1	1588.2	1447.7	1148.6	1069.9	2375
Dark experiment	1956.6	1304.4	1087	1061.7	1014.5	2417

Note S1 Calculation of Dark Evaporation Enthalpy

Since all CPC-series hydrogels are nearly fully hydrated during the solar-driven interfacial evaporation process, the energy required for water evaporation primarily includes the vaporization enthalpy of free water and intermediate water, which is theoretically lower than the value for bulk water. To determine the dark evaporation enthalpy, we designed a control experiment in which each hydrogel sample and pure water (with identical exposed evaporation areas) were placed in sealed, completely dark containers. The environmental conditions were maintained at a constant humidity of 25% and temperature of 21°C. The dark evaporation rate of each sample was then used to estimate the equivalent evaporation enthalpy. As the total energy input into the pure water and hydrogel systems is assumed to be equal in the dark environment, the dark evaporation enthalpy of the hydrogels can be calculated using the following equation:

$$U_{in} = h_1 m_1 = h_2 m_2 \tag{S2}$$

Where h_1 and m_1 are the evaporation enthalpy and mass loss of pure water, respectively, m_2 is the mass loss of the hydrogel sample, h_2 is the calculated dark evaporation enthalpy of the hydrogel.

Note S2 Calculation of Heat Loss

In general, heat loss during the interfacial evaporation process consists of three components: conductive heat loss, convective heat loss, and radiative heat loss. The calculations are as follows:

(1) Conductive heat

$$Q_{cond} = Cm\Delta T_b \tag{S3}$$

Where Q_{cond} is the conductive heat loss, C is the specific heat capacity of water (4.2 kJ °C^{-1} kg^{-1}), m is the mass of water (fixed at 60 g), ΔT_b is the temperature rise of the bulk water.

(2) Convective heat

Convective heat loss is calculated based on Newton's law of cooling:

$$Q_{conv} = hA\Delta T_c \tag{S4}$$

Where Q_{conv} is the convective heat flux, h is the convective heat transfer coefficient (assumed to be ~5 W m^{-2} K^{-1}), A is the evaporation area (fixed at 0.314 × 10^{-3} m^2), ΔT_c is the temperature difference between the material's evaporating surface and the ambient air just above the absorber.

(3) Radiative heat

Radiative heat flux is calculated using the Stefan–Boltzmann equation:

$$\Phi = \varepsilon A\sigma(T_1^4 - T_2^4) \tag{S5}$$

Where Φ is the radiative heat flux, ε is the surface emissivity (assumed to be 1 during evaporation), σ is the Stefan–Boltzmann constant (5.67 × 10^{-8} W m^{-2} K^{-4}), T_1 is the steady-state surface temperature of the hydrogel under one sun irradiation, T_2 is the ambient temperature above the absorber.

Note S3 COMSOL simulation

The heat transfer process during evaporation in CPC-UA and CPC-A was simulated using the Heat Transfer Module in COMSOL Multiphysics 6.3. A three-dimensional model was first constructed in SolidWorks based on the actual dimensions of the laboratory evaporation device and then imported into COMSOL Multiphysics 6.3 for simulation. A constant solar irradiance of 1 kW m^{-2} was applied to the top surface of the evaporator to drive the evaporation process. The inflow water flux into the evaporator was set equal to the outflow caused by evaporation. The boundary conditions were defined as follows: ambient temperature and initial water temperature were both set to 20 °C (293.15 K); the natural convective heat transfer coefficient was set to 5 W m^{-2} K^{-1}; and the solar absorption efficiency was set at 95%. The density, specific thermal conductivity of CPC-UA were 0.2163 g cm^{-3}, 3.137 J g^{-1} K^{-1} and 0.5097 W m^{-1} K^{-1}, respectively. The density, specific thermal conductivity of CPC-A were 0.2011 g cm^{-3}, 3.206 J g^{-1} K^{-1} and 0.4835 W m^{-1} K^{-1}, respectively. Based on these boundary and material parameters, the temperature distribution in the 3D COMSOL model was simulated using the following governing equations:

$$Q_{in}=\rho C_p\frac{\partial T}{\partial t}+\rho C_p u\nabla T+\nabla q \tag{S6}$$

$$q=-k\nabla T \tag{S7}$$

Where Q_{in} is the heat input from solar radiation, ρ, C_p, and k are the material's density, specific heat capacity, and thermal conductivity, respectively, T(x, t) is the local temperature distribution as a function of space and time, u is the fluid velocity vector, q is the heat flux vector. The simulation was carried out under a steady-state analysis mode in COMSOL Multiphysics 6.3. Heat convection at the top surface of the evaporator in contact with air was corrected using Newton's law of cooling.

References

[1] Chen K, Ma L, Shi J, et al. Fumed nano-silica modified PVA-chitosan composite hydrogel with Janus structure for solar-driven interfacial evaporation[J]. Solar Energy, 2024, 281: 112865.

[2] Chu A, Yang M, Chen J, et al. Biomass-enhanced Janus sponge-like hydrogel with salt resistance and high strength for efficient solar desalination[J]. Green Energy & Environment, 2024, 9(11): 1698-1710.

[3] Fan D, Min H, Zhang H, et al. Architecting a bifunctional solar evaporator of

perovskite La0. 5Sr0. 5CoO3 for solar evaporation and degradation[J]. Journal of Materials Science, 2021, 56(33): 18625-18635.
[4] Gong X, Hu F, Tang J, et al. Simultaneous realization of efficient solar evaporation and electricity collection through dual regulation of chemical composition and pore channels[J]. Chemical Engineering Journal, 2024, 501: 157595.
[5] Hao L, Liu N, Bai H, et al. High-performance solar-driven interfacial evaporation through molecular design of antibacterial, biomass-derived hydrogels[J]. Journal of colloid and interface science, 2022, 608: 840-852.
[6] Kang Q, Zhai Y, Zhao F, et al. Salt-resistant and antibacterial polyvinyl alcohol/chitosan/silver-loaded graphene oxide electrospun nanofiber membrane for high-efficiency solar-driven desalination[J]. Chemical Engineering Research and Design, 2024, 205: 107-117.
[7] Li J, Yan L, Li X, et al. Porous polyvinyl alcohol/biochar hydrogel induced high yield solar steam generation and sustainable desalination[J]. Journal of Environmental Chemical Engineering, 2022, 10(3): 107690.
[8] Li Q, Chen D, Jiao X. Double-layer Janus sponge evaporator: Optimal balancing between evaporation efficiency and salt resistance[J]. Chemical Engineering Journal, 2025: 160085.
[9] Liu J, Zhu J, Guo S, et al. In-situ constructing cellulose/PVA hydrogel with confinement capillarity for efficient solar interfacial evaporation[J]. Desalination, 2023, 565: 116855.
[10] Lu Y, Fan D, Wang Y, et al. Surface patterning of two-dimensional nanostructure-embedded photothermal hydrogels for high-yield solar steam generation[J]. ACS nano, 2021, 15(6): 10366-10376.
[11] Meera B, Vidhya C, Nair R B, et al. Sustainable sponge-like composite hydrogel evaporator for highly efficient solar steam generation[J]. Materials Today Sustainability, 2023, 23: 100439.
[12] Ren J, Chen L, Gong J, et al. Hofmeister effect mediated hydrogel evaporator for

simultaneous solar evaporation and thermoelectric power generation[J]. Chemical Engineering Journal, 2023, 458: 141511.

[13] Wilson H M, Lim H W, Lee S J. Highly efficient and salt-rejecting poly (vinyl alcohol) hydrogels with excellent mechanical strength for solar desalination[J]. ACS Applied Materials & Interfaces, 2022, 14(42): 47800-47809.

[14] Wu X, Lin D, Zhou H, et al. Salt crystallization on porous asymmetrical graphene oxide-based photothermal hydrogel-fabric unexpectedly enables continuous solar-powered hypersaline water distillation[J]. Carbon, 2025, 233: 119833.

[15] Xiang Y, Sun Y, Li M, et al. Multi-routes of water migration assisted by hierarchical porous structure for boosting solar-driven evaporation[J]. Chemical Engineering Journal, 2025: 160220.

[16] Xu B, Yao X, Zhang X, et al. A fabric interpenetrating composite hydrospongels with permeability and evaporation enthalpy regulation for efficient solar-driven interfacial evaporation and water purification[J]. Chemical Engineering Journal, 2025, 503: 158642.

[17] Yan J, Chen L, Song X, et al. Mechanically robust and anisotropic hydrogel composites for high efficiency steam generation[J]. Colloids and Surfaces A: Physicochemical and Engineering Aspects, 2024, 703: 135256.

[18] Zhao J, Chu A, Chen J, et al. Spongy polyelectolyte hydrogel for efficient Solar-Driven interfacial evaporation with high salt resistance and compression resistance[J]. Chemical Engineering Journal, 2024, 485: 150118.

[19] Zhu M, Liu X, Tian Y, et al. Dome-arrayed chitosan/PVA hydrogel-based solar evaporator for steam generation[J]. Scientific Reports, 2022, 12(1): 4403.